Dynamics of a flexible helical filament rotating in a viscous fluid near a rigid boundary

M. K. Jawed
Department of Mechanical Engineering, Massachusetts Institute of Technology, Cambridge, Massachusetts 02139, USA

P. M. Reis*
Department of Mechanical Engineering, Department of Civil and Environmental Engineering, Massachusetts Institute of Technology, Cambridge, Massachusetts 02139, USA

(Received 17 August 2016; published 24 March 2017)

We study the effect of a no-slip rigid boundary on the dynamics of a flexible helical filament rotating in a viscous fluid, at low Reynolds number conditions (Stokes limit). This system is taken as a reduced model for the propulsion of uniflagellar bacteria, whose locomotion is known to be modified near solid boundaries. Specifically, we focus on how the propulsive force generated by the filament, as well as its buckling onset, are modified by the presence of a wall. We tackle this problem through numerical simulations that couple the elasticity of the filament, the hydrodynamic loading, and the wall effect. Each of these three ingredients is respectively modeled by the discrete elastic rods method (for a geometrically nonlinear description of the filament), Lighthill's slender body theory (for a nonlocal fluid force model), and the method of images (to emulate the boundary). The simulations are systematically validated by precision experiments on a rescaled macroscopic apparatus. We find that the propulsive force increases near the wall, while the critical rotation frequency for the onset of buckling usually decreases. A systematic parametric study is performed to quantify the dependence of the wall effects on the geometric parameters of the helical filament.

DOI: 10.1103/PhysRevFluids.2.034101

I. INTRODUCTION

Locomotion of microorganisms through the rotation of a flagellum (a slender helical filament) in a viscous fluid is ubiquitous [1,2] and representative of 90% of marine bacteria [3]. During the past two decades, there has been significant progress in understanding flagellar propulsion through experiments [4–7], computation [8–10], and theory [11–14]. The primary challenge in predictively modeling this fluid-structure interaction problem arises from the need to fully couple the geometrically nonlinear structural mechanics of the flagellum with an accurate description of the hydrodynamic loading induced by the viscous fluid. Recent efforts have modeled this system as a Kirchhoff elastic rod [15], coupled to the fluid with resistive force theory (RFT) [16], and established that the flagellum can undergo a buckling instability [10]. However, subsequent experiments have shown that whereas RFT provides a satisfactory qualitative description of the phenomena, an accurate quantitative analysis requires a *nonlocal* hydrodynamic force model that accounts for the interaction between the flow induced by distant parts of the filament [17]. Reference [9] has indeed employed a nonlocal slender body description, coupled with Kirchhoff's theory of rods to study the deformation of a helical rod under rotation or axial flow, but only up to linear order of the deflection [9]. More recently, we have investigated the propulsion and instability (buckling) of a helical elastic rod rotated in a viscous fluid, by a combination of Lighthill's slender body theory (LSBT) [16] and the discrete

*preis@mit.edu

 ©2017 American Physical Society

elastic rods (DER) [18,19] method for a geometrically nonlinear description of the flexible filament [20,21].

Near a boundary, bacterial locomotion can be significantly modified, when compared to swimming in the bulk of a fluid bath [22–27]. For example, *Vibrio alginolyticus*, a uniflagellated bacterium, moves forward and backward by alternating the rotational direction of its flagellum in a zigzag pattern [28]. A rigid boundary modifies this pattern to *run* and *arc* traces; the cells swim linearly during forward motion and curve sharply when moving backward [5]. The effect of boundaries on *Escherichia coli*, a multiflagellated bacterium, has also been investigated in detail. Three-dimensional tracking of its trajectories demonstrated that the swimming speed is changed near a boundary, whose presence also leads to an attractive interaction [22]. Moreover, experiments have also shown that *E. coli* traces clockwise circular paths near solid surfaces [24,27,29].

Hydrodynamic interaction has been suggested as the main mechanism behind the aforementioned experimental observations [24,30]. Theoretical studies that include this interaction date back to almost half a century when Blake [31,32] introduced the method of images for the fundamental solutions of Stokes flow (e.g., the Stokeslet) in the presence of a wall. Based on this method, resistive drag coefficients were developed to approximate the force on a rigid slender body close to a no-slip boundary or between two such boundaries [33]. This method was modified for applications in conjunction with the method of regularized Stokeslets and applied to model a cilium near a boundary [34]. A distinct and more recent numerical approach to the study of wall effects was proposed in Ref. [14], which enhanced the boundary element method for propulsion from a rigid flagellum connected to spherical cell body [35] to include a rigid wall. A review of boundary integral, boundary element, and immersed boundary methods often used in elastohydrodynamic systems can be found in Refs. [36–38].

The theoretical developments and experimental findings mentioned above have paved the way for a number of recent computational and modeling studies for bacterial locomotion near boundaries [12,14,26,39–41]. Additionally, several simplified physical models have been developed to explain specific aspects of the wall effect [12,42]. For example, the circular motion of *E. coli* was explained by an elaborate model consisting of a rigid helical flagellum and a spherical body with the RFT fluid model [24]. Subsequently, a reduced model for a bacterium near boundary, consisting of two spheres of different radii connected by a dragless rod, was used for a quantitative analysis of the circular trajectory [42]. These studies were followed by a more generic model to account for such variety of boundary-driven modifications to flagellar locomotion [13] where an axisymmetric swimmer is described as a linear combination of fundamental solutions to Stokes flow, and the contribution of each singularity is adjusted to account for the wall effects. Numerical methods for the boundary effect coupled with elasticity in spermatozoa [43] and cilia [44] have also been developed.

However, none of the above studies considered a flexible helical flagellum in the presence of a wall. Motivated by the geometric nonlinearities during turning [7], tumbling [45], bundle formation [46], and polymorphic transformations [47,48], we have recently combined precision model experiments with numerical simulations to demonstrate a wealth of interesting dynamics of a slender elastic rod rotating in a viscous fluid. Our findings included a critical angular velocity above which the rod buckles due to excessive fluid loading [20,21]. Scale invariance of the mechanics of this problem allowed us to perform experiments with a macroscopic analog model to inform the original microscopic system. Our numerical tool combined DER [18,19]—a computational tool used in the animation industry for visually dramatic simulation of hair, fur, and other rod-like objects—with LSBT [16]—a framework that models the viscous drag on a slender rod to account for the long-range hydrodynamic interaction between distant parts of the rod. This forms the appropriate foundation to examine wall effects on flexible rods in viscous fluid, which is yet to be addressed.

Here, we systematically explore the effect of a no-slip planar wall on the propulsive force and onset of buckling instability in a helical elastic rod rotating in viscous fluid. We implement a numerical simulation that uses the method of images [31] to include wall effects in our aforementioned framework of DER coupled with LSBT. Precision experiments with a macroscopic analog of the flagellum are performed to validate our simulations. Since the rod is a slender elastic structure,

there is a critical angular velocity above which buckling can occur [10,20]. We analyze the onset of this instability as the distance from the boundary is varied and find excellent agreement between experiments and simulations, without any fitting parameters. We then probe the numerical tool to quantify the propulsive force generated in the presence of a wall and observe increased propulsion as the flagellum gets closer to the boundary. Through systematic sweeps of parameter space in biologically relevant regimes, we identify the enhancement in propulsion in rods similar in geometry to natural flagella, as well as the shift in phase boundary for instability.

Our paper is organized as follows. In Sec. II, we present the basis of the numerical simulations, followed by a description of the experimental setup in Sec. III. In Sec. IV, we compare numerical and experimental results for the onset of instability of the rotating rod, as a function of distance from the boundary. The simulation tool is then probed to quantify the variation in propulsive force. In Sec. V, we then systematically quantify the variation in wall effect with the geometry of the helix, with a focus on biologically relevant regimes. Finally, in Sec. VI, we present our conclusions and suggest potential avenues for future research.

II. NUMERICAL MODEL

We develop a numerical model that combines three components: (i) DER, (ii) LSBT, and (iii) method of images. Whereas each of these three ingredients has been previously investigated on their own (see the literature review in Sec. I), they are used in concert in this study to simulate the deformation of a linear elastic rod of arbitrary geometry due to hydrodynamic forces from a viscous fluid medium, in the presence of a rigid wall. This section is organized as follows. A description of DER is provided in Sec. II A, and its coupling with LSBT in Sec. II B; this coupled framework was introduced in Ref. [20]. In Sec. II C, we detail the procedure to include the method of images for a no-slip wall, which is the primary aspect of the current study. The geometry and boundary conditions of the problem are then discussed in Sec. II D.

A. Discrete elastic rods

We use the DER method [19] to model the helical filament as a linear elastic rod. Kirchhoff's theory of elastic rods [15] represents the centerline of the rod by an arc-length parameterized curve, $\boldsymbol{\gamma}(s)$, and the angular evolution of the tangent-aligned orthonormal material directors by $\theta(s)$. The local strains in the deformed configuration can be captured by the curvature, $\kappa(s) = ||\boldsymbol{\gamma}''(s)||$, twist [evaluated from $\theta'(s)$], and axial stretch. At every time step within the discrete setting employed by DER, based on the balance between the elastic forces and the relevant external forces, the rod configuration is updated. For future numerical implementations, we recommend starting with an existing DER code [49], and adding the boundary conditions and the external forces (detailed in subsequent sections). Details on the numerical procedure that underlies DER can be found in Ref. [19]. In the following, we provide a summary of this method.

1. Kinematic representation

In the discrete setting [see Fig. 1(a)], the discrete curve is composed of $(n+2)$ vertices $\mathbf{x}^0, \ldots, \mathbf{x}^{n+1}$, and $(n+1)$ edges $\mathbf{e}^0, \ldots, \mathbf{e}^n$ such that $\mathbf{e}^i = \mathbf{x}^{i+1} - \mathbf{x}^i$. Each edge, $\mathbf{e}^i$, has an associated material frame $\{\mathbf{m}_1^i, \mathbf{m}_2^i, \mathbf{t}^i\}$ and reference frame $\{\mathbf{d}_1^i, \mathbf{d}_2^i, \mathbf{t}^i\}$. The reference directors, $\mathbf{d}_1^i$ and $\mathbf{d}_2^i$, rotated about the tangent, $\mathbf{t}^i$, by an angle θ^i align with the material directors, $\mathbf{m}_1^i$ and $\mathbf{m}_2^i$. The reference frame, $\{\mathbf{d}_1^i, \mathbf{d}_2^i, \mathbf{t}^i\}$, is a *time-parallel* adapted orthonormal frame; this reference frame is not necessarily the same as the material frame even though they share the tangent, $\mathbf{t}^i$, as one of the directors. This frame stays adapted to the centerline through parallel transport [19] in time. As DER proceeds from one time step to the next, the reference frame is rotated by the minimum amount needed to keep it adapted. The material frame, as well as any other adapted frame, can then be represented by an angle, θ^i, that rotates about the shared tangent, $\mathbf{t}^i$, from the reference to the material frame.

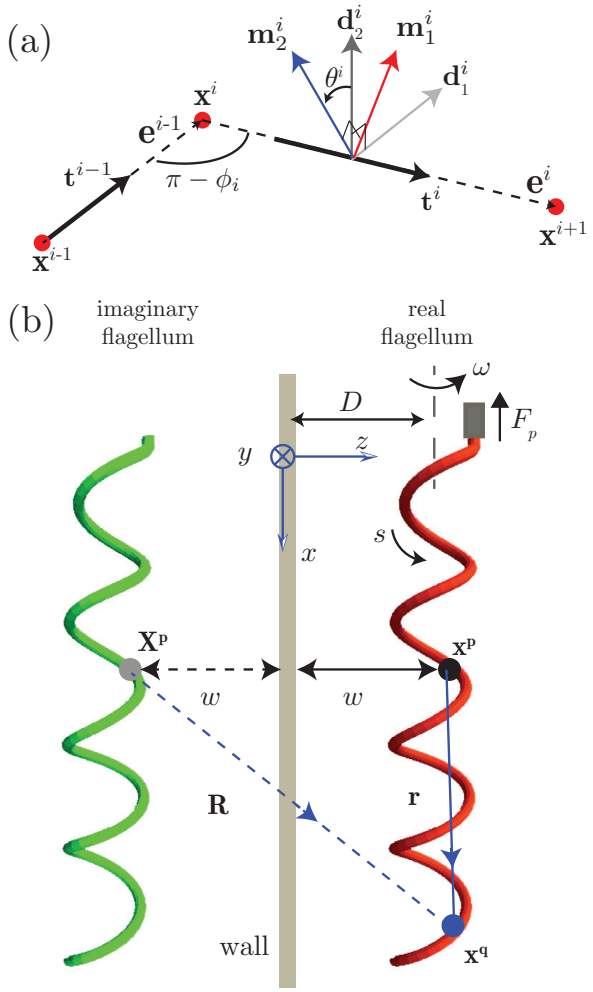

FIG. 1. (a) Discrete rod described by the vertices $\mathbf{x}^i$ (red dots) and edges $\mathbf{e}^i$ (dashed arrows). A reference ($\{\mathbf{d}_1^i, \mathbf{d}_2^i, \mathbf{t}^i\}$) and a material ($\{\mathbf{m}_1^i, \mathbf{m}_2^i, \mathbf{t}^i\}$) frame are associated with each edge, $\mathbf{e}^i = \mathbf{x}^{i+1} - \mathbf{x}^i$. (b) Schematic diagram of the problem used in the numerical simulations. The real flagellum (red) is composed of a series of nodes, $\mathbf{x}^p$, along the arc length parameterized by s. An imaginary flagellum (green) is positioned as a mirror image of the real flagellum about the z axis, such that for each real node, $\mathbf{x}^p = (x^p, y^p, w)$, there is an image node at $\mathbf{X}^p = (x^p, y^p, -w)$. The clamped end of the real flagellum is rotated about the helix axis with a prescribed angular velocity, ω.

At every time step, DER solves for the balance of forces at the following degrees of freedom: $3(n+2)$ nodal coordinates of the vertices, $\mathbf{x}^i$, and $(n+1)$ angular orientations of material frame, θ^i. We now sequentially introduce the strains, elastic energies, and forces in terms of this kinematic representation.

2. *Strains*

The *axial strain* associated with an edge, $\mathbf{e}^j$, is

$$\varepsilon^j = \frac{|\mathbf{e}^j|}{|\mathbf{e}^j|_r} - 1. \tag{1}$$

Hereafter, quantities with subscript r indicate evaluation in the stress-free state.

The material *curvatures* associated with node $\mathbf{x}^i$ are

$$\kappa_i^{(1)} = \tfrac{1}{2}\left(\mathbf{m}_2^{i-1} + \mathbf{m}_2^i\right)(\kappa\mathbf{b})_i, \tag{2a}$$

$$\kappa_i^{(2)} = -\tfrac{1}{2}\left(\mathbf{m}_1^{i-1} + \mathbf{m}_1^i\right)(\kappa\mathbf{b})_i, \tag{2b}$$

where $(\kappa\mathbf{b})_i$ is the curvature binormal,

$$(\kappa\mathbf{b})_i = \frac{2\mathbf{e}^{i-1}\times\mathbf{e}^i}{|\mathbf{e}^{i-1}|_r|\mathbf{e}^i|_r + \mathbf{e}^{i-1}\cdot\mathbf{e}^i}. \tag{3}$$

This quantity is a measure of misalignment between two consecutive edges. If ϕ_i is the turning angle between two consecutive edges [see Fig. 1(a)], the norm of curvature binormal is $|(\kappa\mathbf{b})_i| = \kappa_i = 2\tan(\phi_i/2)$.

The *twist* in the discrete setting associated with edge $\mathbf{e}^i$ at time t_k can be expressed as

$$m^i(t_k) = \Delta\theta_i + \underline{m}^i(t_k), \tag{4}$$

where $\Delta\theta^i = \theta^i(t_k) - \theta^i(t_{k-1})$ and $\underline{m}^i$ is the reference twist associated with the twist of the reference frame [19].

3. Elastic energies

For a rod with Young's modulus, E, and shear modulus, G, the elastic energies—stretching, bending, and twisting—are given by

$$E_s = \frac{1}{2}\sum_{j=0}^{n} EA(\varepsilon^j)^2|\mathbf{e}^j|_r, \tag{5a}$$

$$E_b = \frac{1}{2}\sum_{i=1}^{n}\frac{EI}{l_i}\left\{\left[\kappa_i^{(1)} - \left(\kappa_i^{(1)}\right)_r\right]^2 + \left[\kappa_i^{(2)} - \left(\kappa_i^{(2)}\right)_r\right]^2\right\}, \tag{5b}$$

$$E_t = \frac{1}{2}\sum_{i=1}^{n}\frac{GJ}{l_i}\left(m^i - m_r^i\right)^2, \tag{5c}$$

respectively, where $l_i = \frac{1}{2}(|\mathbf{e}^i|_r + |\mathbf{e}^{i-1}|_r)$ is the vertex-based Voronoi length and A is the area of cross section. We assumed an isotropic homogeneous rod with uniform stretching stiffness EA, bending stiffness EI, and torsional stiffness GJ in the expressions for energy.

4. Elastic forces

Let us denote the degrees of freedom as $\mathbf{q} = (\mathbf{x}^0,\theta^0,\ldots,\mathbf{x}^n,\theta^n,\mathbf{x}^{n+1})^T$, which is a vector of size $4n+7$. For each degree of freedom q_i, the elastic forces (associated with $\mathbf{x}^i$) and elastic moments (associated with θ^i) are

$$F_i = -\frac{\partial}{\partial q_i}(E_s + E_b + E_t), \tag{6}$$

where $0 \leqslant i < 4n+7$. To advance from time step t_k to $t_{k+1} = t_k + \Delta t$, DER applies Newton's method to solve for increments to positions, $\Delta\mathbf{q} = \mathbf{q}(t_{k+1}) - \mathbf{q}(t_k)$, and velocities, $\Delta\dot{\mathbf{q}} = \dot{\mathbf{q}}(t_{k+1}) - \dot{\mathbf{q}}(t_k)$ in the following equations of motion,

$$M\Delta\dot{\mathbf{q}} - \Delta t\,\mathbf{F}[\mathbf{q}(t_k) + \Delta\mathbf{q}] = \Delta t\,\mathbf{F}_{\text{ext}}, \tag{7a}$$

$$\Delta\mathbf{q} - \Delta t\,\Delta\dot{\mathbf{q}} = \Delta t\,\dot{\mathbf{q}}(t_k), \tag{7b}$$

where M is the lumped mass matrix and $\mathbf{F}_{\text{ext}}$ is a vector of size $4n+7$ containing the external forces (associated with $\mathbf{x}^i$) and external moments (associated with θ^i) at time step t_k. For computational

efficiency, the integration scheme in DER is implicit on elastic forces and requires the Hessian of the elastic energy, $J_{ij} = \frac{\partial^2}{\partial q_i \partial q_j}(E_s + E_b + E_t)$, with $0 \leqslant i, j < 4n + 7$.

In this time marching scheme, the external loading on a rod can be included by the $\mathbf{F}_{\text{ext}}$ term in Eq. (7). We consider hydrodynamic loading as an external loading in this study and express this force in terms of the nodal coordinates in the subsequent sections.

B. Lighthill slender body theory

We used LSBT to model the viscous drag experienced by a slender rod in motion within a viscous fluid and couple this into the DER framework described above. A detailed account of the coupling between LSBT and DER can be found in Ref. [20], where we first developed the method and validated it against experiments. In the remainder of this section, we briefly review the LSBT-DER implementation, without yet considering the presence of a wall, which will be introduced in Sec. II C, below.

The primary Green's function (or fundamental singular solution) of Stokes flow is the Stokeslet, which describes the flow associated with a singular point force [32]. Other fundamental solutions can be obtained from its derivatives and are known as rotlets, stresslets, potential doublets, and higher-order poles [50]. Along the centerline of the rod parameterized by the arc-length parameter, s, LSBT assumes a series of Stokeslets and dipoles, and provides a relationship between the local velocity, $\mathbf{u}(s)$, on the centerline and the force per unit length, $\mathbf{f}(s)$,

$$\mathbf{u}(s) = \frac{\mathbf{f}_\perp(s)}{4\pi\mu} + \int_{|\mathbf{r}(s',s)|>\delta} \mathbf{f}(s') \cdot \mathbb{J}(\mathbf{r}) ds', \tag{8}$$

where $\mathbf{f}_\perp(s) = \mathbf{f}(s)[\mathbb{I} - \mathbf{t}(s) \otimes \mathbf{t}(s)]$ is the component of $\mathbf{f}$ in the plane perpendicular to the tangent $\mathbf{t}(s)$, μ is the dynamic viscosity of the fluid, $\mathbf{r}(s',s)$ is the position vector from s' to s, $\delta = r_0\sqrt{e}/2$ is the natural cutoff length (r_0 is the radius of the circular cross section of the rod and e is the Napier's constant), and $\mathbb{J}(\mathbf{r}) = \frac{1}{8\pi\mu}(\frac{\mathbb{I}}{r} + \frac{\mathbf{r}\mathbf{r}^T}{r^3})$ is the Oseen tensor.

In Fig. 1(b), we provide a schematic of the setup of our numerical simulations. We use a discrete version of Eq. (8) to relate the velocity $\mathbf{u}^q$ at node q with the force $\mathbf{f}^p$ on node p,

$$\mathbf{u}^q = \frac{\mathbf{f}^q_\perp}{4\pi\mu\Delta} + \sum_{p=1, p\neq q}^{N} \mathbf{u}_s(\mathbf{r}) \tag{9}$$

where $\Delta = 2\delta$ is the length of each edge in the discrete rod, N is the number of nodes, $\mathbf{r} = \mathbf{x}^q - \mathbf{x}^p$ is position vector from node p to node q, with $\hat{\mathbf{r}} = \mathbf{r}/r$ as the corresponding unit vector, and, the velocity from each Stokeslet is expressed as [32]

$$\mathbf{u}_s(\mathbf{r}) = \frac{1}{8\pi\mu r}[\mathbb{I} + \hat{\mathbf{r}}\hat{\mathbf{r}}^T]\mathbf{f}^p. \tag{10}$$

The relationship between forces and velocities provided by Eq. (9) can be written as a linear system with $1 \leqslant p,q \leqslant N$ (spanning across the nodes) and $1 \leqslant i, j \leqslant 3$ (spanning across three Cartesian dimensions),

$$\mathbf{U} = \mathbf{A}\mathbf{F} \text{ where } \begin{cases} U_{3(q-1)+i} = u_i^q \\ F_{3(p-1)+j} = f_j^p \end{cases}. \tag{11}$$

The matrix $\mathbf{A}$ in Eq. (11) has size $3N \times 3N$ and depends only on the geometric configuration of the rod and is, hereafter, referred to as the *geometry matrix*,

$$A_{3(q-1)+i,3(p-1)+j} = \frac{1}{8\pi\mu} \begin{cases} 2\left(\delta_{ij} - t_i^q t_j^q\right)/\Delta, & \text{if } q = p, \\ \frac{1}{r}(\delta_{ij} + \hat{r}_i \hat{r}_j), & \text{if } q \neq p, \end{cases} \tag{12}$$

where $\delta_{ij} = 1$ for $i = j$ and $\delta_{ij} = 0$ for $i \neq j$. We now have all the ingredients in this fluid-structure interaction problem of a thin rod moving in a viscous fluid to relate the forces applied by the fluid and the velocities along the rod in a discrete setting. At each time step in DER, knowing the velocity of each node on the rod and the nodal coordinates, we can compute the velocities, $\mathbf{U}$, and the geometry matrix, $\mathbf{A}$. We then use the discrete force-velocity relation in Eq. (11) to evaluate the forces, $\mathbf{F}$ (details in Supplemental Material [51]), which, in the next time step, are applied as external forces on the elastic rod to evolve the system in time.

C. Method of images

We now turn to the main contribution of the current study and include the effect of a no-slip wall on the DER-LSBT framework described above. Our goal is to formulate a procedure based on the method of images [31] that will enable us to investigate geometrically nonlinear deformations of a fluid-loaded elastic rod close to a boundary. Interestingly, Lighthill himself mentioned that "[this theorem] *needs to be modified by including with each stokeslet the effects of its image system* [in the presence of] *plane solid boundary*" [16]. This is in congruence with our numerical formulation used in this study.

In the schematic diagram of Fig. 1(b), the wall is located at $z = 0$ (without loss of generality). For each Stokeslet on the centerline of the rod [red (right) rod in Fig. 1(b)], an image system is considered on an *imaginary* mirrored rod [green (left) rod in Fig. 1(b)], with the wall as the mirror plane. The image system for a node at $\mathbf{x}^p = \langle x, y, w \rangle$ is located at $\mathbf{X}^p = \langle x, y, -w \rangle$ and includes (i) a Stokeslet, (ii) a potential dipole, and (iii) a doublet. Due to the slender body approximation, our formulation is valid provided that each node is located at a distance $w \gg \delta$ (or equivalently $w \gg r_0$) away from the boundary.

We proceed by expanding the force-velocity relation in Eq. (9) to include the image system and calculate the velocity at $\mathbf{x}^q$ in terms of the viscous forces applied at $\mathbf{x}^p$, with $1 \leqslant p \leqslant N$ [see Fig. 1(b)]. The radius vector of $\mathbf{x}^q$ with respect to the image system is $\mathbf{R} = \mathbf{x}^q - \mathbf{X}^p$, and the corresponding unit vector is $\hat{\mathbf{R}} = \mathbf{R}/R$. The resulting relationship between velocities and forces acting on node q reads [31]

$$\mathbf{u}^q = \frac{\mathbf{f}^q_\perp}{4\pi\mu\Delta} + \sum_{p=1, p\neq q}^{N} [\mathbf{u}_s(\mathbf{r}) - \mathbf{u}_s(\mathbf{R}) - \mathbf{u}_{pd}(\mathbf{R}) + \mathbf{u}_{sd}(\mathbf{R})], \tag{13}$$

where the velocity from the Stokeslet $\mathbf{u}_s(\mathbf{r})$ was provided in Eq. (10); the velocity from the image Stokeslet is [31]

$$\mathbf{u}_s(\mathbf{R}) = \frac{1}{8\pi\mu R}[\mathbb{I} + \hat{\mathbf{R}}\hat{\mathbf{R}}^T]\mathbf{f}^p; \tag{14}$$

the velocity from potential dipole is [31]

$$\mathbf{u}_{pd}(\mathbf{R}) = \frac{w^2}{4\pi\mu R^3}[\mathbb{I} - 3\hat{\mathbf{R}}\hat{\mathbf{R}}^T]\mathbf{q}^p; \tag{15}$$

with $\mathbf{q}^p = \langle -f_1^p, -f_2^p, f_3^p \rangle$, and finally the velocity from Stokes doublet is [31]

$$\mathbf{u}_{sd}(\mathbf{R}) = \frac{2w}{8\pi\mu R^2}\left[\hat{\mathbf{s}}\mathbf{e}_3^T + (\mathbf{e}_3 \cdot \hat{\mathbf{R}})\mathbb{I} - \mathbf{e}_3\hat{\mathbf{R}}^T - 3(\mathbf{e}_3 \cdot \hat{\mathbf{R}})\hat{\mathbf{R}}\hat{\mathbf{R}}^T\right]\mathbf{q}^p. \tag{16}$$

As an illustration of the implementation of the computational framework introduced above, we start by providing a two-dimensional (2D) example, prior to presenting fully three-dimensional

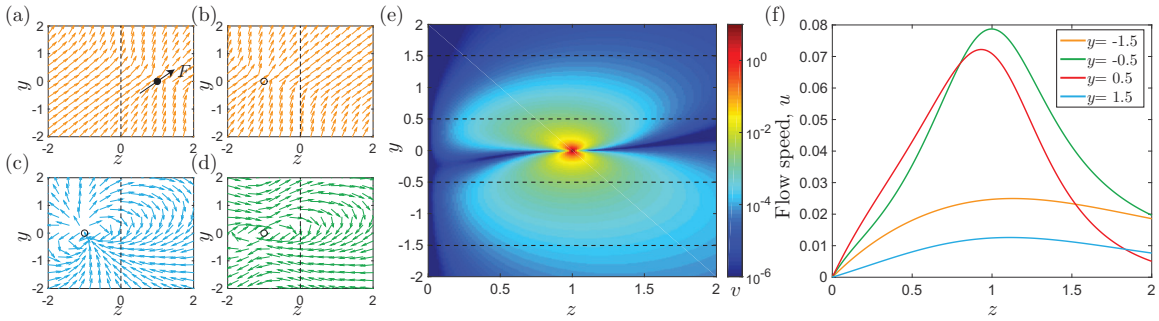

FIG. 2. Flow field generated by the relevant fundamental solutions in a two-dimensional space, (x,y). Direction of the fluid velocity from (a) Stokeslet on real node [Eq. (10)], (b) Stokeslet on imaginary node [Eq. (14)], (c) potential dipole [Eq. (15)], and (d) doublet [Eq. (16)]. (e) Magnitude of the velocity field, $\sqrt{u_y^2+u_z^2}$, given by Eq. (13) upon superposition of the solutions from panels (a)–(d). (f) Norm of the velocity, $u=\sqrt{u_y^2+u_z^2}$, as a function of z at four different values of y indicated by the dashed lines in panel (e). This plot confirms that the velocity at $z=0$ is always zero as required for a no-slip boundary.

results. In 2D, for any point, $\mathbf{x}^q$, that is not a node of the rod, the velocity from Eq. (13) reduces to

$$\mathbf{u}^q = \sum_{p=1}^{N} [\mathbf{u}_s(\mathbf{r}) - \mathbf{u}_s(\mathbf{R}) - \mathbf{u}_{pd}(\mathbf{R}) + \mathbf{u}_{sd}(\mathbf{R})]. \tag{17}$$

This result derives from the fact that Lighthill's approximation [16] implies that the first term in the expression for velocity $\mathbf{u}^q$ in Eq. (13) is relevant only up to a distance $\delta < r_0$ from the node. If the point is on the wall, i.e., $x_3^q = 0$, Eq. (17) yields $\mathbf{u}^q = 0$. To illustrate this, we consider a single Stokeslet (i.e., $N=1$) of strength $\mathbf{f}^p = \langle 0,1,1\rangle$ (chosen arbitrarily) located at a distance of unit length from the wall ($\mathbf{x}^q = \langle 0,0,1\rangle$) and its image system. For simplicity, the viscosity is here assumed to be unity ($\mu = 1$). In Figs. 2(a)–2(d), we draw the four contributions to the velocity field $\mathbf{u}^q$, corresponding to the four individual terms in Eq. (17): $\mathbf{u}_s(\mathbf{r}), \mathbf{u}_s(\mathbf{R}), \mathbf{u}_{pd}(\mathbf{R})$, and $\mathbf{u}_{sd}(\mathbf{R})$. The arrows of the vector field in this figure represent the direction of the velocity, which, for clarity, have all been normalized to have the same length. In Fig. 2(e), we have superposed the four contributions from Figs. 2(a)–2(d), now with actual value of their magnitude, where the adjacent color bar represents the norm of the total velocity, $u = |\mathbf{u}^q| = \sqrt{u_y^2+u_z^2}$. We observe that $\mathbf{u}^q$ reduces to 0 on the wall. To further attest the vanishing velocity at the wall, in Fig. 2(f), we plot the norm of velocity, u, as a function of z, at four different values of the vertical position $y = \{-1.5,-0.5,0.5,1.5\}$, all of which are indeed found to decay to $u=0$ on the wall ($z=0$). This simple example involving a single Stokeslet illustrates how the image system enforces zero velocity on the boundary.

We now proceed to the case of multiple Stokeslets distributed along the arc length of a three-dimensional rod. In the presence of the boundary, the formulation for the geometry matrix $\mathbf{A}$ in Eq. (11) is

$$A_{3(q-1)+i,3(p-1)+j} = \frac{1}{8\pi\mu} \begin{cases} 2\left(\delta_{ij} - t_i^q t_j^q\right)/\Delta, & \text{if } q = p, \\ \frac{1}{r}(\delta_{ij} + \hat{r}_i \hat{r}_j) + A^{img}_{3(q-1)+i,3(p-1)+j}, & \text{if } q \neq p, \end{cases} \tag{18}$$

where A^{img} is the contribution from the image system and, upon algebraic manipulation, can be written as [40]

$$A^{img}_{3(q-1)+i,3(p-1)+j} = \frac{1}{8\pi\mu}\left[-\frac{1}{R}(\delta_{ij} + \hat{R}_i \hat{R}_j) + 2w \sum_{k=1}^{3} \delta'_{jk} \frac{\partial}{\partial R_k} \frac{1}{R}\left(\frac{w}{R}\hat{R}_i - \delta_{i3} + \hat{R}_i \hat{R}_3\right)\right], \tag{19}$$

with

$$\delta'_{jk} = \begin{cases} 1, & \text{if } j = k = 1,2, \\ -1, & \text{if } j = k = 3, \\ 0, & \text{if } j \neq k. \end{cases} \tag{20}$$

The matrix, A^{img}, can be interpreted as an extension of the Blake tensor [31] representing the velocity fields in Stokes flow due to a point force near a stationary plane boundary.

This completes the formulation of the fluid loading of the slender rod, in the presence of a wall, that can now be readily implemented in conjunction with DER. In summary, at the end of every time step in DER, we evaluate the vector **U** in the discrete force-velocity relation of Eq. (11) from the velocity at each node and the geometry matrix **A** [Eq. (18)] calculated from the configuration of the rod. The force vector, **F**, can then be computed by solving the linear system $\mathbf{U} = \mathbf{AF}$ in Eq. (11). While solving this linear system, and to avoid numerical issues associated with the inversion, we assume that the force varies smoothly along s [51]. Without this assumption (or other appropriate preconditioning), the solution to Eq. (11) may be physically implausible. Finally, the external force on each node can be obtained from **F** in Eq. (11), and is then applied in the subsequent time step of DER.

D. Definition of the problem

The general framework introduced above for the coupling between DER-LSBT, including the method of images, is now applied to the specific problem of a helical elastic filament, rotated in a viscous bath, near a no-slip rigid wall. Next, we provide specifics on the geometry and physical parameters of this problem. The slender filament (reduced analog model of a flagellum) is taken to be a right-handed helical rod, made out of a linear elastic material (Young's modulus E and Poisson's ratio ν), with pitch, λ, and helix radius, r_h, in its stress-free configuration. The helical filament is clamped at one extremity, where it is rotated anticlockwise (from above) with a prescribed angular velocity, ω, and free at the other. The axis of the helix in the stress-free configuration is at a distance D from a no-slip rigid wall located at $z = 0$. Hereafter, we normalize the boundary distance by the axial length of the helical rod, l, such that the normalized distance is $\bar{D} = D/l$. The rotation is imposed by prescribing the nodal coordinates of the first two nodes such that $\mathbf{x}^0 = \langle x_r^0, r_h \sin(\omega t), r_h \cos(\omega t) + D \rangle$ and $\mathbf{x}^1 = \langle x_r^1, r_h \sin(\omega t), r_h \cos(\omega t) + D \rangle$, where x_r^0 and x_r^1 are the x coordinates of these nodes at $t = 0$. The orientation of the material frame, θ^0, is also constrained such that the twist in $\mathbf{e}^0$ is zero. The remaining degrees of freedom of the discrete rod are considered free. Further details on this boundary condition can be found in Ref. [20]. In this model system, the net force generated by the rotation of the rod is canceled at the clamp by an equal and opposite reaction force. In natural bacteria, however, the flagellum generates a propulsive force that is used to move the cell body forward, and together the system is force free.

The geometric and material parameters of the rod were chosen to match the laboratory experiments described in Sec. III, and the results are generalized using a nondimensionalization procedure introduced later in this section. Unless otherwise stated, the physical parameter values of the rod are rod density, $\rho_r = 1.273\,\mathrm{g/cm^3}$; Young's modulus $E = 1255 \pm 49\,\mathrm{kPa}$; Poisson's ratio $\nu \approx 0.5$ (incompressible); radius of circular cross section, $r_0 = 1.58 \pm 0.02$ mm (and, therefore, second moment of inertia, $I = \pi r_0^4/4$); axial length, $l = 14.64 \pm 0.1\,\mathrm{cm}$; normalized pitch, $\lambda/l = 0.236$; and normalized radius, $r_h/l = 0.0542$. The viscosity of the fluid was $\mu = 2.7 \pm 0.12\,\mathrm{Pa\,s}$, and its density was $\rho_m = 1.24\,\mathrm{g/cm^3}$. A small density mismatch ($\rho_r > \rho_m$) and the resulting buoyant force were included to emulate the fact that this effect is present in the experiments detailed in Sec. III. The angular velocity of rotation at the clamp was varied in the range $0 \leqslant \omega\,[\mathrm{rad/s}] < 2$, such that, throughout the study, the Reynolds number was $\mathrm{Re} = \rho\omega r_h r_0/\mu < 2 \times 10^{-2}$, i.e., always in the Stokes limit. In this representative setup, the number of nodes along the discrete rod is 109 corresponding to an edge length of Δ introduced in Eq. (9). The time step size in the simulation was $\leqslant 5 \times 10^{-4}$ s after a convergence study.

Due to the slender geometry of the system, bending is the prominent mode of deformation of the rod. The characteristic flexural force is EI/l^2 and the viscous drag scales as $\mu\omega l^2$ (alternatively, $\mu \mathbf{u} l$). A balance between the elastic bending force and the external viscous loading yields the characteristic time scale $\mu l^4/(EI)$, which is used to nondimensionalize the angular velocity as

$$\bar{\omega} = \omega \mu l^4/(EI), \tag{21}$$

velocities as

$$\bar{\mathbf{u}} = \mathbf{u} \mu l^3/(EI), \tag{22}$$

and time as

$$\bar{t} = tEI/(\mu l^4). \tag{23}$$

Equation (21) can also be written as $\bar{\omega} = (l/l_\omega)^4$, where $l_\omega = [EI/(\mu\omega)]^{1/4}$ is the penetration length [52,53]. This dimensionless representation employed herein allows for generality across length scales in the interpretation of our findings. The dimensionless representation of angular velocity, $\bar{\omega}$, and velocity, $\bar{\mathbf{u}}$, has been previously verified in Refs. [20,21].

In all of the numerical simulations reported in this study, the first two nodes of the rod near the clamping point have prescribed motion to mimic an angular velocity and the rotation of the first edge is constrained, for consistency with a clamped end. All other nodes and edges are free and evolve based on the balance between elastic and fluid forces. This setup is similar to that used in our prior work [20,21], except for the presence of a no-slip rigid boundary, which is the interesting aspect of the current study.

In Figs. 3(a1)–3(a4), we present a representative example of our numerical results by showing snapshots of the dynamical evolution of the configuration of a helical rod (parameters defined above), rotated at $\bar{\omega} = 341$, at a normalized distance $\bar{D} = 0.342$ from the boundary. For this specific set of parameters, and as a result of the fluid loading, the originally helical rod [Fig. 3(a1)] is distorted [Fig. 3(a2)] and eventually buckles [Figs. 3(a3)–3(a4)]. The material strain is the largest near the clamped end and decays to zero at the free end of the rod [51]. We had previously studied the conditions for onset of this buckling instability [20], without the presence of a wall, due to excessive viscous loading. For the remainder of this study, we will investigate how this fluid-structure interaction problem is modified by adding a no-slip rigid wall to the system.

In Figs. 3(b1)–3(b4), we present the corresponding flow fields (on the y-z plane at $x = l/2$; the solid line is the projection of the deformed rod on (y,z) plane) associated with the deformation shown in Figs. 3(a1)–3(a4). The color represents the norm of the normalized velocity, $\bar{u} = [\bar{u}_x^2 + \bar{u}_y^2 + \bar{u}_z^2]^{1/2}$, at each point $(x = l/2, y, z)$. Initially [Fig. 3(b1), $\bar{t} = 0$], the helix is axisymmetric with a circular projection on the (y,z) plane. As the originally helical rod deforms, the circle is distorted and undergoes a dramatic change in shape as a consequence of buckling [Figs. 3(b3) and 3(b4)]. When a portion of the rod crosses or moves close to the $x = l/2$ plane, the flow velocity in the adjacent region increases, and results in the bright spots corresponding to higher velocity in the flow fields of Figs. 3(b2) and 3(b3). The presence of the wall at $z = 0$ leads to a nonaxisymmetric flow field, and the velocity at the wall decays to zero, similarly to the two-dimensional example presented in Figs. 2(e) and 2(f). The time required to reach the buckled state is quantified in the Supplemental Material [51].

These numerical simulations will now be validated by comparing the computed shapes of the helical filament against the deformation measured in precision laboratory experiments, which are described next.

III. EXPERIMENTAL SETUP

In Fig. 4, we present a photograph of the desktop-sized experimental apparatus that we have used to validate the numerical simulations developed in Sec. II. We have previously used a similar setup [20], albeit without the ability to systematically vary the distance, D, between the clamping

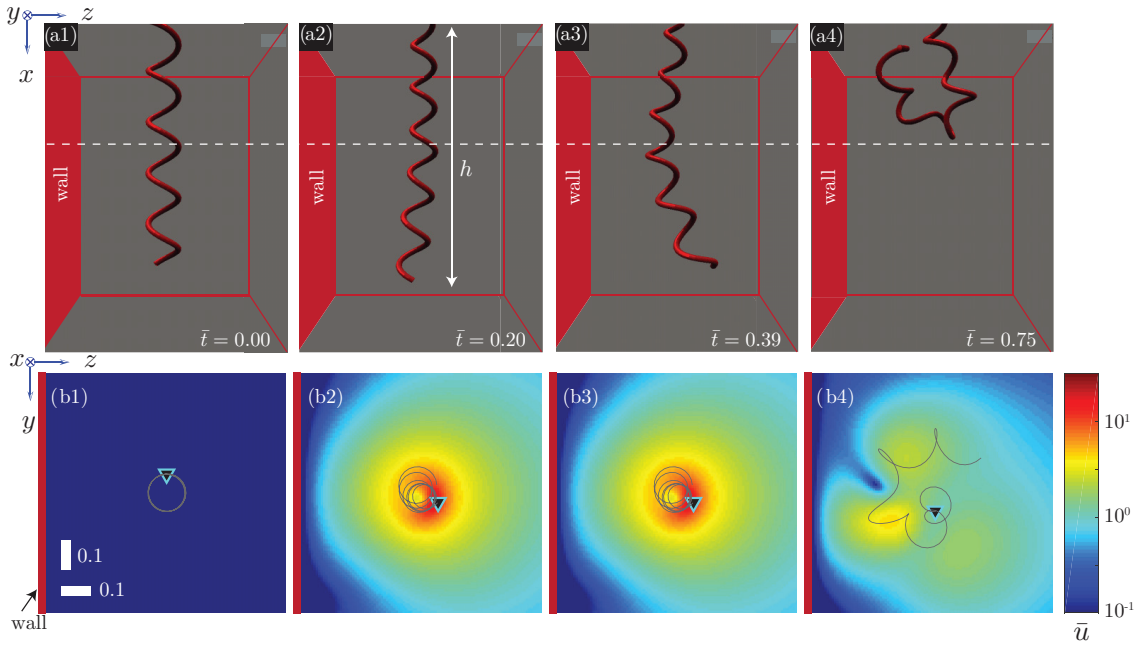

FIG. 3. (a) Rendering of the time evolution of the configuration of a rotating helical rod with normalized angular velocity, $\bar{\omega} = 341$, obtained from the simulations: (a1) $\bar{t} = 0$, (a2) $\bar{t} = 0.20$, (a3) $\bar{t} = 0.39$, and (a4) $\bar{t} = 0.75$. (b) Flow field on the y-z plane at $x = l/2$, with the adjacent color bar indicating the normalized norm of velocity, $\bar{u}$. The solid line is the projection of the centerline of the deformed rod on the (y,z) plane, and the solid triangle represents the location of the clamped end. The horizontal and vertical scale bars correspond to $\bar{x} = x/l = 0.1$ and $\bar{y} = y/l = 0.1$ (where l is the total axial length of the filament). The geometric and material parameters of the rod are described in the text. The distance from boundary is $\bar{D} = 0.342$.

point of the helical filament and one of the side boundaries (the effects of which were originally not considered given the overall large size of the enclosing tank).

The helical rods were fabricated by casting using vinylpolysiloxane (a two-part elastomer: $E = 1255 \pm 49$ kPa and $\nu \approx 0.5$) to obtain well-defined and customizable geometric parameters: cross-

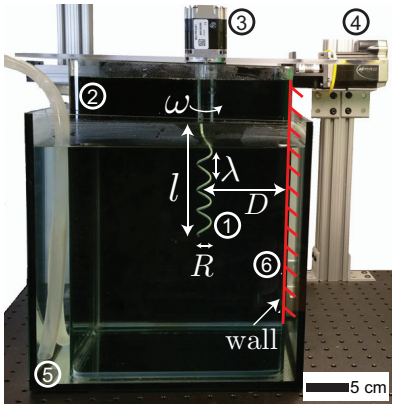

FIG. 4. Photograph of the experimental apparatus. A rod (1) is immersed in a glycerin tank (2) and rotated using a stepper motor (3). A second stepper motor (4) controls the distance, D, between the helix axis and one of the walls. The glycerin tank is placed inside a temperature-controlled water tank (5). The right-hand side (6) of the glycerin tank marked with solid red lines is the boundary considered in this study.

sectional radius, $r_0 = 0.158 \pm 0.002$ cm, axial length, $l = 14.64 \pm 0.1$ cm, pitch, $\lambda = 3 \pm 0.1$, and helix radius, $r_h = 0.794 \pm 0.05$ cm. Details for the protocol employed to fabricate these rods can be found in Refs. [54]. During casting, iron fillings were added to the polymer, in order to increase the density and match it with the density of glycerin $\rho_m = 1.24\,\mathrm{g/cm^3}$ (details on the glycerin bath are provided below). Despite our best efforts in this density matching, our rods had a slightly higher value $[(\rho - \rho_m)/\rho_m \lesssim 0.019]$, which is, however, included in the numerical simulations.

During an experimental test, an individual rod was immersed in a bath of glycerin ($35 \times 24 \times 24\,\mathrm{cm^3}$ along x, y, and z axes, respectively), clamped at one end, and rotated using a stepper motor (NEMA 27). This stepper motor was in turn attached to a linear translator stage (Thomson Industries) driven by a second stepper motor, which allowed for precision control of the distance, D, between the clamping point (and hence the axis of the undeformed helix) and one of the side walls of the tank. The viscosity of glycerin, μ, used in our experiments varies by an order of magnitude ($0.5 < \mu\,[\mathrm{Pa\,s}] < 4.5$) as the temperature is changed between $5 < \theta\,[^\circ\mathrm{C\,s}] < 30$. As such, the glycerin bath was enclosed by an external water tank, which was itself connected to a temperature control unit (Brinkmann Lauda RC6) to set the temperature, T, within $\Delta T = 1.0\,^\circ\mathrm{C}$. All experiments were performed at $T = 11.0 \pm 1.0\,^\circ\mathrm{C}$ ($\mu = 2.7 \pm 0.12\,\mathrm{Pa\,s}$). The temperature (and, therefore, viscosity) of the glycerin was logged every 15 min and used to nondimensionalize the angular velocity according to Eq. (21) to reduce the temperature effects, as stated in Sec. II D.

IV. WALL EFFECT ON THE PROPULSION AND INSTABILITY OF THE HELICAL ROD

Towards validating the numerical simulations presented in Sec. II, we now perform a direct quantitative comparison with experimental results using the apparatus described in Sec. III. Emphasis is given to the deformation of the helical rod due to the combined effect of fluid loading and the nearby wall. For the purpose of this comparison between computed and experimental configurations of the rod, we define its normalized height, $\bar{h} = h/h_0$, where h is the suspended height (vertical distance between clamp and the bottom-most part of the rod) and h_0 is the axial length of the helix at $\bar{\omega} = 0$. This length, h_0, may include buoyancy effects that will make $h_0 \neq l$.

In Fig. 5(a), we plot $\bar{h}$ as a function of $\bar{\omega}$, for two different values of normalized boundary distance $\bar{D} = \{0.143, 0.273\}$, obtained from experiments (open symbols) and simulations (solid lines). For the simulations, we also present the data in the absence of a boundary, i.e., $\bar{D} = \infty$. Given the finite size of the box, a boundary is always present in experiments and $\bar{D}$ is finite. Previously, for the case without a boundary we found that there is a critical value for the rotational velocity, $\bar{\omega}_b$ (normalized buckling velocity), above which the suspended height decreases dramatically [20]. Moreover, the critical torque for buckling of a flagellum (without a wall) was numerically quantified in Ref. [10] using RFT. When a wall is present, we observe similar dynamics and the occurrence of buckling, albeit at different values of $\bar{\omega}_b$, which we quantify next.

In both experiments and simulations, as the distance from the clamp to the boundary is decreased from $\bar{D} = 0.273$ to $\bar{D} = 0.143$, the normalized buckling velocity decreases by 7.1% and 5.8%, respectively. Compared with the no-wall case in simulations, $\bar{\omega}_b$ is reduced by 1.9% at $\bar{D} = 0.273$ and 7.5% at $\bar{D} = 0.143$. These findings indicate an enhanced propensity for buckling in the vicinity of a boundary. In the case of both $\bar{D} = 0.143$ and $\bar{D} = 0.273$, the rod touches the wall upon buckling. We leave a contact model in simulations for future studies. In the experiments, we observe that the rod becomes self-tangled at $\bar{D} = 0.143$ due to contact with the wall and the suspended height oscillates within $0.3 \leqslant \bar{h} \leqslant 0.6$.

Even though both experiments and simulations show the same trend of decreasing ω_b when the distance to the boundary is reduced, our experiments are affected by experimental artifacts that we discuss next. We attribute the mismatch in the measured $\bar{\omega}_b$ values between experiments and simulations to experimental uncertainties associated with manufacturing and in the measurements of the physical properties of the helical rods. Due to these experimental imperfections, we observe that the normalized height remains slightly below $\bar{h} < 1.0$ in the unbuckled regime ($\bar{\omega} < \bar{\omega}_b$), whereas, in simulations, the helix extends along its axial direction to reach $\bar{h} \approx 1.05$ prior to buckling. Moreover,

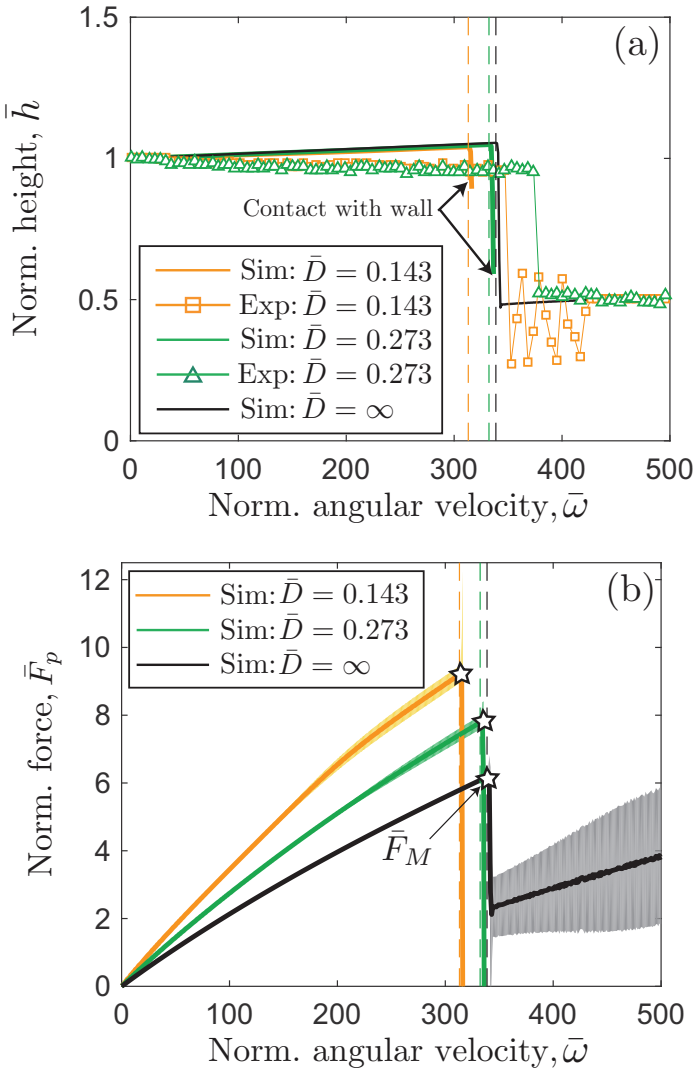

FIG. 5. (a) Steady-state values of the normalized suspended height, $\bar{h}$, as a function of normalized angular velocity $\bar{\omega}$, at three different values of the boundary distance, $\bar{D} = \{0.143, 0.273, \infty\}$, from experiments and simulations (see legend). The normalized buckling velocity, $\bar{\omega}_b$, from the simulations is represented by the vertical dashed lines. (b) Normalized propulsive force, $\bar{F}_p$, as a function of $\bar{\omega}$ obtained from the numerical simulations. The shaded region corresponds to the standard deviation of the force signal.

in the experiments, we find that the rod undergoes small sideways undulations, in contrast with an almost uniform extension in simulations. This interpretation is consistent with the well-known fact that buckling of slender structures is highly sensitive to system imperfections. The approximations invoked in LSBT [16] and the slender rod assumption may also contribute to this mismatch. Further comparison between our experiments and simulations is presented later in this section.

The propulsive force (equal to the reaction force at the clamp) and torque (applied by the motor on the rod) of this macroscopic setup is too small to be measured experimentally [20]. Therefore, we leverage our simulations to quantify the effect of the rigid boundary on propulsion. As the rod is rotated in the viscous bath, this propulsive force is generated along the negative x axis, $F_p = -\int_0^L \mathbf{f}(s) \cdot \mathbf{e}_x ds$, where $L = l/\cos(2\pi r_h/\lambda)$ is the contour length of the rod and $\mathbf{e}_x$ is the unit vector along x axis. Without a wall, we had previously found that F_p increases with angular velocity up to a maximum, F_M, at the onset of buckling ($\bar{\omega} = \bar{\omega}_b$), after which it drops sharply [20]. We now want to investigate how F_p is modified as a function of the distance between the helical

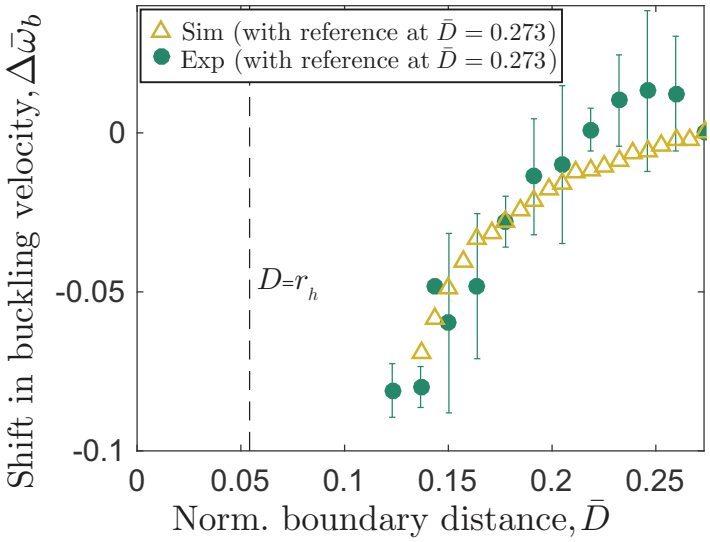

FIG. 6. Shift in buckling velocity, $\Delta\bar{\omega}_b$, as a function of normalized boundary distance, $\bar{D}$, from experiments (closed symbols) and simulations (open symbols), with respect to the reference value of $\bar{D} = 0.273$. For $D < r_h$, the rod contacts the wall and this region is therefore not considered.

filament and the wall. In Fig. 5(b), we plot the normalized propulsive force $\bar{F}_p = F_p l^2/(EI)$, as a function of $\bar{\omega}$, for three values of $\bar{D}$. Similarly to the no-wall case ($\bar{D} = \infty$), when a rigid boundary is present, $\bar{F}_p$ increases up to a normalized maximum propulsive force, $\bar{F}_M$ [represented by the star symbols in Fig. 5(b)], just before $\bar{\omega}_b$. As $\bar{D}$ is decreased, the onset of buckling occurs earlier ($\bar{\omega}_b$ is decreased), even if the corresponding value of $\bar{F}_M$ increases. For example, when $\bar{D} = 0.143$ (or $\bar{D} = 0.273$), the maximum propulsive force, $\bar{F}_M$, is increased by 49% (or 27%) compared to the no-wall case. Note that even though the propulsive force is along the negative x axis, the helical rod slightly extends in simulations prior to buckling. This counterintuitive observation is explained in Supplemental Material [51].

Next, we perform a systematic investigation of the effect of the distance to the wall on propulsion and the onset of buckling, which will also act as a validation of the numerical simulations through comparisons with experiments. For this purpose, we define the following two nondimensional quantities to measure the relative shift due to wall effects on the critical buckling velocity

$$\Delta\bar{\omega}_b = \left(\omega_b - \omega_b^r\right)/\omega_b^r, \tag{24}$$

and the maximum propulsive force,

$$\Delta\bar{F}_M = \left(F_M - F_M^r\right)/F_M^r, \tag{25}$$

where ω_b^r and F_M^r are reference values. It is important to note that, in the experiments, these reference values cannot be accurately determined for the no-boundary ($\bar{D} = \infty$) case, given that the glycerin tank has a finite size and, even if distant, walls are always present. Therefore, for a first comparison with experiments, we chose to use the case with $\bar{D} = 0.273$ (i.e., $D = 4\,\text{cm}$) as reference. This choice was based on the size of our $24 \times 24 \times 35\,\text{cm}^3$ glycerin tank. At $D = 4\,\text{cm}$ away from the side wall under consideration, the other three side walls are {20, 12, 12} cm away from the rod, while the top surface and bottom wall are approximately 17.5 cm distant from the centroid of the rod. As such, we assume that the effect of these other walls is small. Upon validation of these results, we will then move to studying the numerical simulations alone, taking $D = \infty$ as the reference.

In Fig. 6, we plot $\Delta\bar{\omega}_b$ as a function of the normalized distance from the boundary, $\bar{D}$, with the reference assumed at $\bar{D} = 0.273$ for both experiments (filled symbols) and simulations (open symbols), and find excellent agreement between the two. When the boundary distance is $D < r_h$,

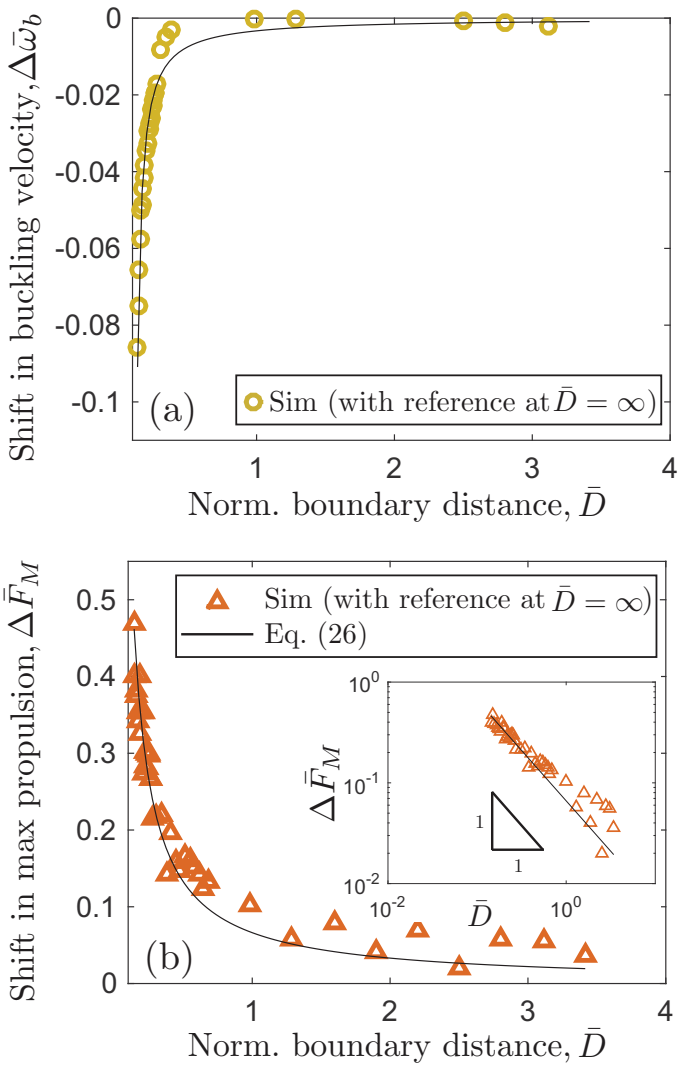

FIG. 7. (a) Simulation data for shift in buckling velocity, $\Delta\bar{\omega}_b$ [Eq. (24)], as a function of normalized boundary distance, $\bar{D}$. (b) Increase in maximum propulsive force, ΔF_M [Eq. (25)], as a function of $\bar{D}$. The reference value is assumed to be at $\bar{D} = \infty$ (i.e., no-wall case). Inset: same data plotted in log-log scale. Solid line represents the fit of Eq. (26) to the data.

the helical rod touches the wall (marked by a vertical dashed line in Fig. 6), which is not taken into account in the simulations. Moreover, we require that the distance between every node on the rod and the wall is large enough, such that the cross-sectional radius is smaller than any another geometric length scale in the system, $r_0 \ll w$, an underlying assumption of our numerical framework. Taking these constraints into consideration, both our experiments and simulations are, therefore, performed for $\bar{D} > 0.1$. We find that, as the rotating helical filament is brought closer to the wall, the critical buckling velocity decreases with respect to the reference value, such that $\Delta\bar{\omega}_b$ is increasingly negative when $\bar{D}$ decreases. The error bars correspond to the standard deviation of $\Delta\bar{\omega}_b$. The good agreement between experiments and simulations further validates our numerical tool, which we now probe to systematically investigate propulsion in the presence of a wall.

In Fig. 7(a), we plot these same quantities ($\Delta\bar{\omega}_b$ versus $\bar{D}$), now only for the simulations, and taking $\bar{D} = \infty$ as the reference value. We find a scenario that is qualitatively similar to the experimental case discussed above (with $\bar{D} = 0.273$ as reference). When the rod is away from the wall and $\bar{D}$ is large, the relative shift due to wall effects, $\Delta\bar{\omega}_b$, is close to zero. Below $\bar{D} \lesssim 1$, this shift in

buckling velocity is reduced sharply. Turning now to the maximum propulsive force, in Fig. 7(b) we plot simulation data for the relative shift in propulsion force $\Delta\bar{F}_M$ (also with $D = \infty$ as reference) and find that the maximum propulsive force increases significantly as the helical filament is rotated closer to the wall. For example, when $\bar{D} \approx 0.2$, $\bar{F}_M$ is 50% larger than the reference (no-wall case), which highlights the strong hydrodynamic effects that a wall can induce in the propulsion. We also find that the shift in maximum propulsion force versus the distance to the wall is relatively well described by empirical power law

$$\Delta\bar{F}_M = \frac{C_F}{\bar{D}}, \tag{26}$$

where $C_F = (6.6 \pm 0.3) \times 10^{-2}$ is a numerical constant evaluated from fitting the data [solid line in Fig. 7(b)]. Recall that in our current study, the axis of the helical rod is oriented parallel to the boundary. For a rigid helical rod, Ref. [14] showed that even though an organism swimming parallel to plane boundaries achieves a propulsive advantage, the swimming speed decreases for an orientation normal to and toward a plane boundary. Our framework is applicable to a planar boundary of arbitrary orientation; however, the effect of boundary orientation and the presence of a cell body on propulsion is beyond the scope of this study and we leave a more systematic investigation of this point for future work.

V. DEPENDENCE OF WALL EFFECTS ON THE GEOMETRY OF THE HELICAL FILAMENT

Thus far, our findings on the enhancement of propulsion and reduction of the onset of buckling due to the presence of a rigid wall have focused on a single geometry as a representative case. Next, we perform a broader exploration of the parameter space for the geometry of the filament, with an emphasis on the ranges that are relevant to natural helical flagella. Given that the buckling velocity scales as $\omega_b \sim EI/(\mu l^4)$ and assuming that the effect of the slenderness ratio, r_0/l, on the flow field is negligible [20], $\Delta\bar{\omega}_b$ and $\Delta\bar{F}_M$ are solely governed by the following dimensionless groups: $\bar{D}$, r_h/l, and λ/l. All these three parameters are geometric and specify the shape of the rod.

We now employ our numerical simulations to explore the effect of $(\lambda/l, r_h/l)$ on the shifts in buckling velocity and maximum propulsive force. In this section, we decide to keep the boundary distance fixed at $\bar{D} = 0.2$ (i.e., $D = 3$ cm), for which we showed in the previous section that there are significant wall effects. The rationale for this choice is that the lower bound is $D = r_h$ (when the helix touches the wall) and we also want to maintain $w \gg r_0$ between every node on the rod and the wall, to ensure validity of our framework, while seeing a large enough effect. The choice of $\bar{D} = 0.2$ fulfills all these criteria throughout the range of rod geometry in the parameter sweep. Moreover, E, r_0, l, and μ are kept fixed at the parameter values of the representative setup. For generality, herein we assume that the density of the fluid equals that of the rod to ignore any buoyant effects. The uncertainties reported in the plots of Fig. 8 correspond to error estimated in the solution of the inverse problem of Eq. (11). A detailed account of the protocol followed to calculate ω_b and to determine the uncertainties associated with the shifts, $\Delta\bar{\omega}_b$ and $\Delta\bar{F}_M$, are discussed in the Supplemental Material [51].

In Fig. 8(a1), we plot the relative shift in buckling velocity, $\Delta\bar{\omega}_b$, as a function of the normalized pitch, λ/l, with the normalized radius fixed at $r_h/l = 0.0542$ (representative case). We find that the shift in buckling velocity decreases as the pitch increases. Interestingly, at low enough values of normalized pitch ($\lambda/l < 0.12$), $\Delta\bar{\omega}_b$ is positive, i.e., buckling velocity, ω_b, is higher in the presence of a boundary at $\bar{D} = 0.2$ compared with the no-wall case. We now turn to the effect of helix radius on the shift in buckling velocity, $\Delta\bar{\omega}_b$. In Fig. 8(a2), we plot $\Delta\bar{\omega}_b$ versus the normalized radius, r_h/l, at the fixed value of the pitch $\lambda/l = 0.236$ (representative case). As the radius increases, $\Delta\bar{\omega}_b$ slightly decreases; however, the effect is moderate with $\Delta\bar{\omega}_b \sim 10\%$. Overall, in the presence of a wall, buckling tends to occur (except at very low values of pitch) at a lower value of $\bar{\omega}_b$ so that $\Delta\bar{\omega}_b < 0$. Physically, this can be attributed to the added drag effect from the wall. A no-slip boundary, in effect, slows down the flow field by enforcing zero velocity, and this in turn allows for

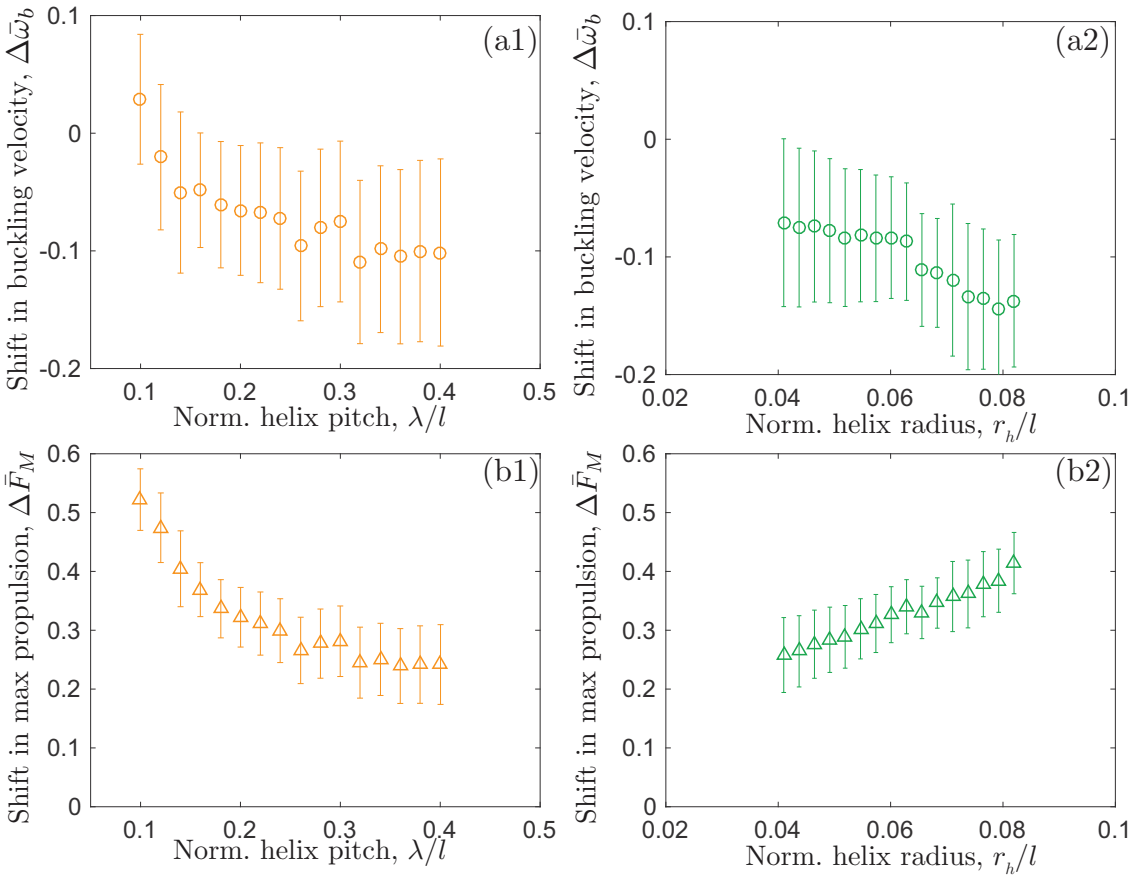

FIG. 8. (a) Shift in buckling velocity, $\Delta\bar{\omega}_b$ [Eq. (24)], at $\bar{D} = 0.2$, as a function of (a1) the normalized pitch, λ/l, at $r_h/l = 0.0542$, and (a2) the normalized radius, r_h/l, at $\lambda/l = 0.236$. (b) Shift in maximum propulsive force, $\Delta\bar{F}_M$ [Eq. (25)], at $\bar{D} = 0.2$ as a function of (b1) the normalized pitch, λ/l, at $r_h/l = 0.0542$, and (b2) the normalized radius, r_h/l, at $\lambda/l = 0.236$. The error bars correspond to the uncertainty stemming from the solution to Eq. (11) [51].

the rod to reach the critical force for buckling at a lower angular velocity. This effect depends on both the geometry of the rod as well as its distance from boundary as evidenced by our results in Figs. 8(a1), 8(a2), and 7.

Regarding the effect of a boundary on the propulsive force, in Fig. 8(b1), we plot $\Delta\bar{F}_M$ versus λ/l at a fixed normalized radius of $r_h/l = 0.0542$ for the same data set used in Fig. 8(a1). As the pitch is increased from $\lambda/l = 0.1$ to $\lambda/l = 0.4$, the shift in maximum propulsion decreases monotonically from $\Delta\bar{F}_M \sim 50\%$ to $\Delta\bar{F}_M \sim 25\%$. In Fig. 8(b2), we present $\Delta\bar{F}_M$ as a function of the normalized radius, r_h/l, while fixing the pitch at $\lambda/l = 0.236$. This same data set was used in Fig. 8(a2). The shift in maximum propulsion increases with increasing radius and reaches $\Delta\bar{F}_M \sim 40\%$ at $r_h/l \sim 0.08$. Within the parameter space explored, our model flagellum, by swimming close to a wall, can attain a propulsive force that is 25–50% higher, when compared to doing so in the fluid bulk. To physically interpret this observation, we note from Fig. 5(b) that, at a fixed value of ω, the propulsive force increases as the rod is set to rotate closer to the wall. However, the wall effect tends to decrease the critical buckling velocity [see Figs. 8(a1) and 8(a2)], and thereby *cuts off* the propulsive force, $\bar{F}_p$, at a lower angular velocity. These two opposing effects determine the increase in maximum propulsive force, $\Delta\bar{F}_M$, which is found to be always positive in the regime explored here. Furthermore, the wall effect on both $\Delta\bar{\omega}_b$ and $\Delta\bar{F}_M$ is more pronounced at higher values of helix radius. Note that the nodes on a rod with radius, r_h, can reach a distance $w = D - r_h$ from the boundary when a perfectly helical rod is rotating about its axis. For a fixed value of boundary

distance a rod with a higher helix radius therefore traverses closer to a boundary (with a lower w) and experiences stronger wall effect.

Altogether, these results emphasize the prominent role of the geometry of the helical filament in its interaction between the wall and the rod. Since the geometry of natural flagella varies significantly between bacterial species [1], our results open up questions on how microorganisms may potentially take advantage from such wall effect.

VI. CONCLUSION

We have introduced a computational framework to simulate the geometrically nonlinear deformation of an elastic rod moving in a viscous fluid near a no-slip planar boundary. For this purpose, our numerical approach combined DER, LSBT, and the method of images. Empowered by this simulation tool, we studied the dynamics of a helical rod undergoing rotation, next to a boundary that is parallel to the axis of the filament. We have quantified the dependence of the onset of the propulsive force and the onset of buckling on the distance to the wall. The simulations were validated using macroscopic model experiments by comparing the relative shift in critical buckling velocity as a function of the boundary distance. To realize the importance of the rod geometry, the simulation tool was then employed to sweep through parameter space along two geometric parameters (helix pitch and radius) and quantify the wall effect. Our results showed that the critical buckling velocity is typically lowered in the presence of a wall, while the maximum propulsive force is enhanced. The scale invariance of this problem suggests the same effect should be present at the microscopic scales relevant to flagellated bacteria.

The significant effect of flagellum geometry, flexibility, and the presence of a wall on the propulsion and instability poses a nontrivial design space for nature. This may have implications in path planning and selection of swimming direction in flagellated microorganisms. Our findings may also provide guidelines for the design of laboratory experiments on bacterial propulsion, e.g., the appropriate size of the fluid reservoir to minimize disturbance from boundaries. Since we used a long-range hydrodynamic force model, our framework may also, eventually, be extended to study multiflagellated systems (self-contact may become important and will need to be incorporated in that case). The effect of the wall on bundling and tumbling behavior [27] may then be explored. The flexibility of the DER framework can be used to include different models for hydrodynamic forces. Provided the similarity in structural mechanics and hydrodynamic forces in cilia [55], our framework could also be readily applied to investigate ciliary locomotion. We hope that our results will inspire and instigate future work on all these fronts, especially to motivate new biophysics experiments with microorganisms.

ACKNOWLEDGMENTS

We are grateful for financial support from the National Science Foundation (CMMI-1129894). We thank Eitan Grinspun (Columbia University) for help with computing resources.

[1] M. Silverman and M. I. Simon, Bacterial flagella, Annu. Rev. Microbiol. **31**, 397 (1977).

[2] E. Lauga and T. R. Powers, The hydrodynamics of swimming microorganisms, Rep. Prog. Phys. **72**, 096601 (2009).

[3] E. Leifson, B. J. Cosenza, R. Murchelano, and R. C. Cleverdon, Motile marine bacteria I: Techniques, ecology, and general characteristics, J. Bacteriol. **87**, 652 (1964).

[4] L. Turner, W. S. Ryu, and H. C. Berg, Real-time imaging of fluorescent flagellar filaments, J. Bacteriol. **182**, 2793 (2000).

[5] S. Kudo, N. Imai, M. Nishitoba, S. Sugiyama, and Y. Magariyama, Asymmetric swimming pattern of *Vibrio alginolyticus* cells with single polar flagella, FEMS Microbiol. Lett. **242**, 221 (2005).

[6] M. Fujii, S. Shibata, and S.-I. Aizawa, Polar, peritrichous, and lateral flagella belong to three distinguishable flagellar families, J. Mol. Biol. **379**, 273 (2008).

[7] K. Son, J. S. Guasto, and R. Stocker, Bacteria can exploit a flagellar buckling instability to change direction, Nat. Phys. **9**, 494 (2013).
[8] R. Cortez, The method of regularized stokeslets, SIAM J. Sci. Comput. **23**, 1204 (2001).
[9] M. J. Kim and T. R. Powers, Deformation of a helical filament by flow and electric or magnetic fields, Phys. Rev. E **71**, 021914 (2005).
[10] R. Vogel and H. Stark, Motor-driven bacterial flagella and buckling instabilities, Eur. Phys. J. E **35**, 15 (2012).
[11] D. Lopez and E. Lauga, Dynamics of swimming bacteria at complex interfaces, Phys. Fluids **26**, 071902 (2014).
[12] A. P. Berke, L. Turner, H. C. Berg, and E. Lauga, Hydrodynamic Attraction of Swimming Microorganisms by Surfaces, Phys. Rev. Lett. **101**, 038102 (2008).
[13] S. E. Spagnolie and E. Lauga, Hydrodynamics of self-propulsion near a boundary: Predictions and accuracy of far-field approximations, J. Fluid Mech. **700**, 105 (2012).
[14] M. Ramia, D. L. Tullock, and N. Phan-Thien, The role of hydrodynamic interaction in the locomotion of microorganisms, Biophys J. **65**, 755 (1993).
[15] G. Kirchhoff, Ueber das Gleichgewicht und die Bewegung eines unendlich dünnen elastischen Stabes, J. Reine Angew. Math. **1859**, 285 (1859).
[16] J. Lighthill, Flagellar hydrodynamics, SIAM Rev. **18**, 161 (1976).
[17] B. Rodenborn, C.-H. Chen, H. L. Swinney, B. Liu, and H. P. Zhang, Propulsion of microorganisms by a helical flagellum, Proc. Natl. Acad. Sci. USA **110**, E338 (2013).
[18] M. Bergou, M. Wardetzky, S. Robinson, B. Audoly, and E. Grinspun, Discrete elastic rods, ACM Trans. Graph. **27**, 63 (2008).
[19] M. Bergou, B. Audoly, E. Vouga, M. Wardetzky, and E. Grinspun, Discrete viscous threads, ACM Trans. Graph. **29**, 116 (2010).
[20] M. K. Jawed, N. K. Khouri, F. Da, E. Grinspun, and P. M. Reis, Propulsion and Instability of a Flexible Helical Rod Rotating in a Viscous Fluid, Phys. Rev. Lett. **115**, 168101 (2015).
[21] M. K. Jawed and P. M. Reis, Deformation of a soft helical filament in an axial flow at low reynolds number, Soft Matter **12**, 1898 (2016).
[22] P. D. Frymier, R. M. Ford, H. C. Berg, and P. T. Cummings, Three-dimensional tracking of motile bacteria near a solid planar surface, Proc. Natl. Acad. Sci. USA **92**, 6195 (1995); P. D. Frymier and R. M. Ford, Analysis of bacterial swimming speed approaching a solid–liquid interface, AIChE J. **43**, 1341 (1997).
[23] Y. Magariyama, M. Ichiba, K. Nakata, K. Baba, T. Ohtani, S. Kudo, and T. Goto, Difference in bacterial motion between forward and backward swimming caused by the wall effect, Biophys. J. **88**, 3648 (2005).
[24] E. Lauga, W. R. DiLuzio, G. M. Whitesides, and H. A. Stone, Swimming in circles: Motion of bacteria near solid boundaries, Biophys. J. **90**, 400 (2006).
[25] P. Galajda, J. Keymer, P. Chaikin, and R. Austin, A wall of funnels concentrates swimming bacteria, J. Bacteriol. **189**, 8704 (2007); J. Hill, O. Kalkanci, J. L. McMurry, and H. Koser, Hydrodynamic Surface Interactions Enable *Escherichia Coli* to Seek Efficient Routes to Swim Upstream, Phys. Rev. Lett. **98**, 068101 (2007).
[26] D. Giacché, T. Ishikawa, and T. Yamaguchi, Hydrodynamic entrapment of bacteria swimming near a solid surface, Phys. Rev. E **82**, 056309 (2010).
[27] M. Molaei, M. Barry, R. Stocker, and J. Sheng, Failed Escape: Solid Surfaces Prevent Tumbling of *Escherichia Coli*, Phys. Rev. Lett. **113**, 068103 (2014).
[28] Y. Magariyama, S.-y. Masuda, Y. Takano, T. Ohtani, and S. Kudo, Difference between forward and backward swimming speeds of the single polar-flagellated bacterium, Vibrio alginolyticus, FEMS Microbiol. Lett. **205**, 343 (2001).
[29] R. Di Leonardo, D. Dell-Arciprete, L. Angelani, and V. Iebba, Swimming with an Image, Phys. Rev. Lett. **106**, 038101 (2011).
[30] O. Sipos, K. Nagy, R. Di Leonardo, and P. Galajda, Hydrodynamic Trapping of Swimming Bacteria by Convex Walls, Phys. Rev. Lett. **114**, 258104 (2015) .
[31] J. R. Blake, A note on the image system for a stokeslet in a no-slip boundary, Math. Proc. Cambridge Philos. Soc. **70**, 303 (1971).

[32] J. R. Blake and A. T. Chwang, Fundamental singularities of viscous flow, part I: The image systems in the vicinity of a stationary no-slip boundary, J. Eng. Math. **8**, 23 (1974).
[33] D. F. Katz, J. R. Blake, and S. L. Paveri-Fontana, On the movement of slender bodies near plane boundaries at low Reynolds number, J. Fluid Mech. **72**, 529 (1975).
[34] J. Ainley, S. Durkin, R. Embid, P. Boindala, and R. Cortez, The method of images for regularized stokeslets, J. Comput. Phys. **227**, 4600 (2008).
[35] N. Phan-Thien, T. Tran-Cong, and M. Ramia, A boundary-element analysis of flagellar propulsion, J. Fluid Mech. **184**, 533 (1987).
[36] C. Pozrikidis, *Boundary Integral and Singularity Methods for Linearized Viscous Flow* (Cambridge University Press, Cambridge, UK, 1992).
[37] T. Y. Hou, J. S. Lowengrub, and M. J. Shelley, Boundary integral methods for multicomponent fluids and multiphase materials, J. Comput. Phys. **169**, 302 (2001).
[38] C. S. Peskin, The immersed boundary method, Acta Numer. **11**, 479 (2002).
[39] E. L. Bouzarth and M. L. Minion, Modeling slender bodies with the method of regularized stokeslets, J. Comput. Phys. **230**, 3929 (2011).
[40] D. J. Smith, A. A. Smith, and J. R. Blake, Mathematical embryology: The fluid mechanics of nodal cilia, J. Eng. Math. **70**, 255 (2011).
[41] T. Goto, T. Nakai, and K. Aoki, Boundary element analysis on transition of distance and attitude of a bacterium near a rigid surface, J. Biomech. Sci. Eng. **5**, 329 (2010).
[42] J. Dunstan, G. Miño, E. Clement, and R. Soto, A two-sphere model for bacteria swimming near solid surfaces, Phys. Fluids **24**, 011901 (2012).
[43] T. D. Montenegro-Johnson, H. Gadelha, and D. J. Smith, Spermatozoa scattering by a microchannel feature: An elastohydrodynamic model, R. Soc. Open Sci. **2**, 140475 (2015).
[44] S. Gueron and K. Levit-Gurevich, Computation of the internal forces in cilia: Application to ciliary motion, the effects of viscosity, and cilia interactions, Biophys. J. **74**, 1658 (1998).
[45] R. M. Macnab and M. K. Ornston, Normal-to-curly flagellar transitions and their role in bacterial tumbling: Stabilization of an alternative quaternary structure by mechanical force, J. Mol. Biol. **112**, 1 (1977).
[46] M. T. Brown, B. C. Steel, C. Silvestrin, D. A. Wilkinson, N. J. Delalez, C. N. Lumb, B. Obara, J. P. Armitage, and R. M. Berry, Flagellar hook flexibility is essential for bundle formation in swimming *Escherichia coli* cells, J. Bacteriol. **194**, 3495 (2012).
[47] C. R. Calladine, Construction of bacterial flagella, Nature (London) **255**, 121 (1975).
[48] N. C. Darnton and H. C. Berg, Force-extension measurements on bacterial flagella: Triggering polymorphic transformations, Biophys. J. **92**, 2230 (2007).
[49] DER source code that implements the elastic sewing machine is available at http://www.cs.columbia.edu/cg/elastic_coiling/
[50] A. T. Chwang and T. Wu, Hydromechanics of low-Reynolds-number flow, part 2: Singularity method for Stokes flows, J. Fluid Mech. **67**, 787 (1975).
[51] See Supplemental Material at http://link.aps.org/supplemental/10.1103/PhysRevFluids.2.034101 for details on the method to obtain forces from velocities, quantification of strains along a rotating rod, discussion on the extension of helix under rotation, and the procedure to measure buckling velocity in simulations.
[52] S. Y. Tony, E. Lauga, and A. E. Hosoi, Experimental investigations of elastic tail propulsion at low Reynolds number, Phys. Fluids **18**, 091701 (2006).
[53] A. A. Evans and E. Lauga, Propulsion by passive filaments and active flagella near boundaries, Phys. Rev. E **82**, 041915 (2010).
[54] A. Lazarus, J. T. Miller, and P. M. Reis, Continuation of equilibria and stability of slender elastic rods using an asymptotic numerical method, J. Mech. Phys. Solids **61**, 1712 (2013); J. T. Miller, A. Lazarus, B. Audoly, and P. M. Reis, Shapes of a Suspended Curly Hair, Phys. Rev. Lett. **112**, 068103 (2014); A. Lazarus, J. T. Miller, M. M. Metlitz, and P. M. Reis, Contorting a heavy and naturally curved elastic rod, Soft Matter **9**, 8274 (2013).
[55] C. Brennen and H. Winet, Fluid mechanics of propulsion by cilia and flagella, Annu. Rev. Fluid Mech. **9**, 339 (1977).

"Dynamics of a flexible helical filament rotating in a viscous fluid near a rigid boundary" — Supplemental Information —

M.K. Jawed, P. M. Reis

M. K. Jawed

S1 Evaluation of forces from velocities

As explained in detail in the manuscript, our computational tool combines the Discrete Elastic Rods (DER) method (for the elasticity of the rod), Lighthill's slender body theory (for the fluid force model), and the method of images (to emulate the boundary). At every time step, we evaluate the fluid forces, f, from the velocities, u, at each of the N nodes of the rod. For convenience, we reproduce the relation between force versus velocity, Eq. (11), in the manuscript:

$$\mathbf{U} = \mathbf{A}\mathbf{F} \text{ where } \begin{cases} U_{3(q-1)+i} = u_i^q \\ F_{3(p-1)+j} = f_j^p \end{cases} . \tag{S1}$$

In this linear system, $1 \leq p, q \leq N$ (spanning across the nodes) and $1 \leq i, j \leq 3$ (spanning across three Cartesian dimensions). The matrix $\mathbf{A}$ has size $3N \times 3N$, and its expression is provided in the main text. We have to solve the inverse problem of computing the forces represented by $\mathbf{F}$ knowing the matrix $\mathbf{A}$ and velocities represented by $\mathbf{U}$. While solving this linear system, we follow the strategy below to avoid numerical issues.

It is assumed that the force varies smoothly along the arc-length of the rod, s, such that f_j^p can be expressed in terms of *reduced forces*, f_j^{*r}, where $1 \leq r \leq N^*$. The number of reduced forces, N^*, was chosen to be $\sim N/3$; the rationale behind this choice is discussed later in this section. Also, define $b = N/N^*$. The forces in terms of the reduced forces are written as

$$f_j^p = \sum_{r=1}^{N^*} \frac{N - (b\,r - p)}{N} f_j^{*r}. \tag{S2}$$

This allows us to write the force vector $\mathbf{F}$ as

$$\mathbf{F} = \mathbf{C}\mathbf{F}^*, \tag{S3}$$

where $F^*_{3(r-1)+j} = f_j^{*r}$ and $\mathbf{C}$ is a $3N \times 3N^*$ sized matrix. The entries of the matrix $\mathbf{C}$ can be computed from Eq. (S2). The force versus velocity relation of Eq. (S1) can now be written as

$$\mathbf{U} = \mathbf{A}^*\mathbf{F}^*, \text{ where } \mathbf{A}^* = \mathbf{A}\mathbf{C}, \tag{S4}$$

which is solved using singular value decomposition (SVD) to obtain F^*. The force vector, $\mathbf{F}$, can then be readily obtained from Eq. (S3).

S1.1 Error evaluation.

The error, E, associated with our solution procedure can be estimated from

$$E = \frac{||\mathbf{U} - \mathbf{A}\mathbf{F_s}||}{||\mathbf{U}||}, \tag{S5}$$

where $\mathbf{F_s}$ is our solution to Eq. (S1), and $||\cdot||$ corresponds to the Frobenius norm. This error usually decreases as the number of reduced forces, N^*, increases. However, computational costs increase with increasing N^*. We observed that $N^* \sim N/3$ yields an error of $E \lesssim 5\%$ at a reasonable computational cost. The uncertainty in our measurements of critical buckling velocity, ω_b, and maximum propulsive force, F_M, was estimated to be the mean of this error, E, across all the time steps. For all the results presented in the manuscript, we maintained an uncertainty of $\lesssim 5\%$. Moreover, we used propagation of error to estimate the uncertainty in the shift in buckling velocity, $\Delta\bar{\omega}_b$, and the shift in maximum propulsive force, $\Delta\bar{F}_M$. This uncertainty is shown as errorbars in Fig. 8 of the manuscript.

S2 Strains induced by viscous loading

In this section, we quantify the strains induced in our rotating elastic rods at low Reynolds number. In Fig. 3 of the main text, we provided a representative example of the dynamic evolution of the configuration of a helical rod with normalized angular velocity, $\bar{\omega} = 341$, and normalized boundary distance, $\bar{D} = 0.34$. The three modes of elastic deformation in a Kirchhoff elastic rod are stretching, bending, and twisting. Following the description in §II.A of the manuscript, an axial strain, $|\varepsilon^j|$, is associated with each edge with index j. For each internal node with index i $(0 < i < n + 1)$, the curvature, κ^i, and twist angle, m^i, can also be computed. This curvature and twist correspond to a maximum bending strain, $\varepsilon_b^i = |\kappa^i - \kappa_r^i|r_0/\Delta$, and a maximum twisting strain, $\varepsilon_t^i = |m^i - m_r^i|r_0/\Delta$, respectively, where r_0 is the cross-sectional radius, Δ is the length of an edge, and subscript r indicates evaluation of the quantity in stress-free configuration.

In Figs. S1(a), we reproduce the configurations of the rod undergoing deformation from Fig. 3(a) of the main text. Figs. S1(b) show the strain measures corresponding to these configurations as functions of the

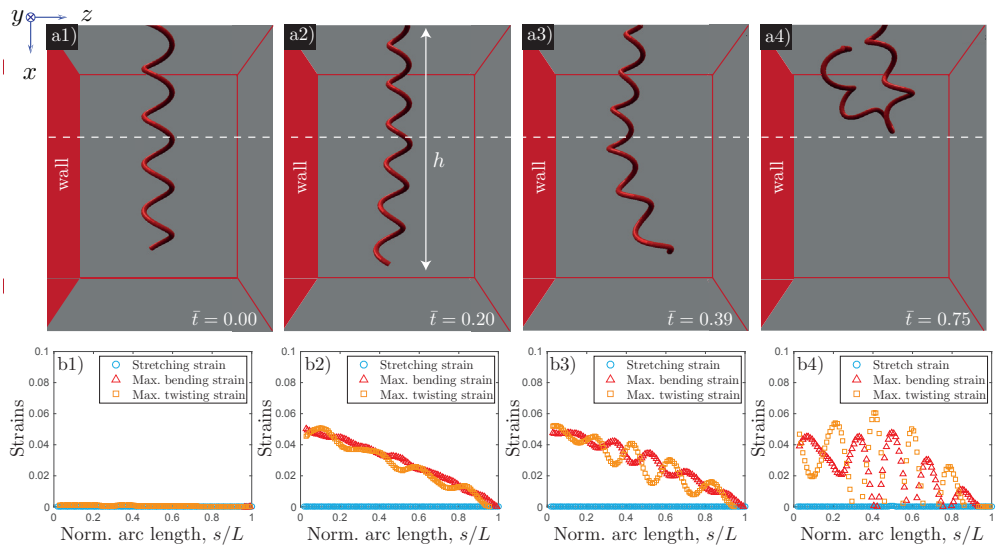

Figure S1: (a) Rendering of the time-evolution of the configuration of a rotating helical rod with normalized angular velocity, $\bar{\omega} = 341$, obtained from the simulations: (a1) $\bar{t} = 0$, (a2) $\bar{t} = 0.20$, (a3) $\bar{t} = 0.39$, and (a4) $\bar{t} = 0.75$. (b) Stretching, maximum bending, and maximum twisting strains as functions of normalized arc length, s/L. Material, geometric, and fluid parameters are provided in the main text.

arc length, s, normalized by contour length, L. The axial strain is negligible compared with the bending and twisting strains. The maximum values of bending and twisting strains always remain $\lesssim 5\%$. The strains are the highest near the clamp ($\bar{s} = 0$), and decays to zero near the free end ($\bar{s} = 1$).

We now average these strain measures along the arc length to obtain the mean stretching strain, $\sum_j |\varepsilon^j|$, mean maximum bending strain, $\sum_i |\varepsilon_b^i|$, and mean maximum twisting strain, $\sum_i |\varepsilon_t^i|$. Fig. S2 shows these mean strain measurements as functions of time. We perform additional simulations without considering a wall (all other parameters remain unchanged), and plot the strains (dashed lines) in the same figure. In both cases, we find that the mean bending and twisting strains increase to $\sim 3\%$, and then show a transient response ($0.5 \lesssim \bar{t} \lesssim 1$ with wall and $0.75 \lesssim \bar{t} \lesssim 1.25$ without wall) to eventually reach $\sim 2\%$.

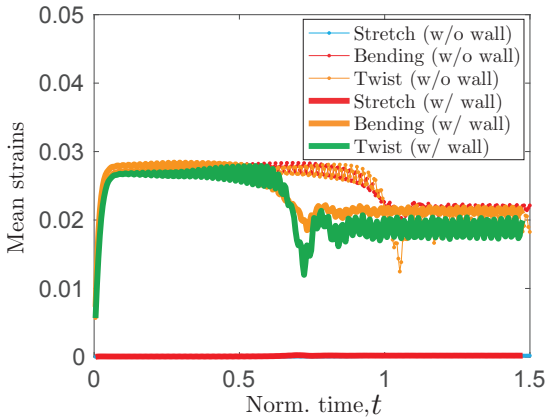

Figure S2: Mean of the strain measures – stretching, maximum bending, and maximum twisting – as a function of normalized time, $\bar{t}$.

S3 Extension of a helical rod under rotation

In Fig. 5 of the manuscript, we found that when a right-handed helical rod is rotated counter-clockwise (viewed from above), it extends along the axial direction even though the propulsive force is along the negative x-axis (see Fig. S3 for the definition of the coordinate system). In this section, we provide a rationale for this counter intuitive observation.

We start by considering the representative case of the manuscript without any boundaries and rotate the rod at an angular velocity of $\omega = 5$ rpm. In Fig. S3(a), a schematic of the helix is shown. At each node of the helix, $\mathbf{x}^i = \langle x^i, y^i, z^i \rangle$, we consider a radial vector, $\mathbf{r}^i$, directed from this node to the helix axis, on $y - z$ plane, such that $\mathbf{r}^i = \langle 0, -y^i, -z^i \rangle$. The surrounding fluid exerts a viscous force, $\mathbf{f}^i$, at each node and we compute its radial component, $f_r = \mathbf{r}^i \cdot \mathbf{f}^i$. In Fig. S3(b), at time $t = 50$ s (arbitrarily chosen), we plot (top panel) the radial force per unit length, along the arc-length of the helix, as well as (bottom panel) the propulsive component of the force. Recall from the main text that the propulsive force is defined as the component of the external viscous force along negative x-axis. We find that both the propulsive and the radial forces are on the same order of magnitude, and, therefore, the radial force can have a significant contribution to the dynamics of the system.

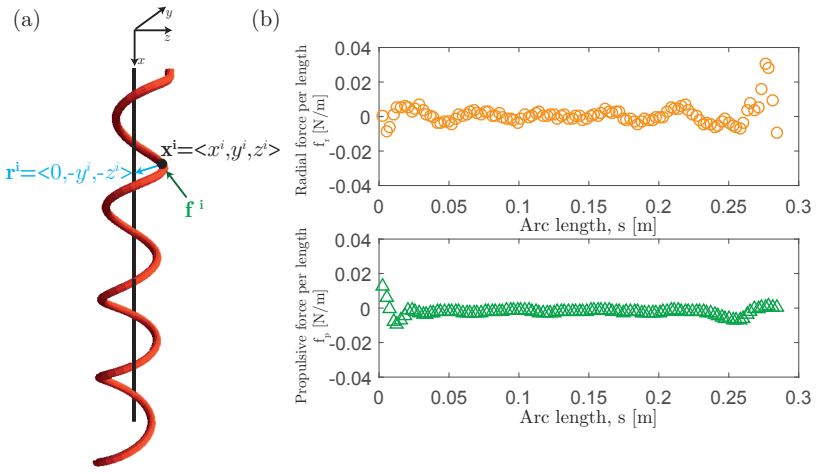

Figure S3: (a) Schematic showing the helix with its axis coinciding with x-axis. On each node, $\mathbf{x}^i = \langle x^i, y^i, z^i \rangle$, a viscous force, $\mathbf{f}^i$, is applied. The radial component to that force is $f_r^i = \mathbf{f}^i \cdot \mathbf{r}^i$, where $\mathbf{r}^i = \langle 0, -y^i, -z^i \rangle$ is the radial vector (from the node towards the helix axis). (b) At $t = 50$ s, the radial force, f_r, (per unit length) vs. the arc length parameter, s, (top) and the propulsive force, f_p, vs. s (bottom).

We can define a quantity "total radial force" (sum of the radial force along the arc length), $F_r = \sum_i f_r^i$, where i spans all nodes. In Fig. S4, F_r is plotted as a function of time. Note that the radial force is positive (beyond the transient period of $t \sim 10$ seconds), which is consistent with the finding that the helix can slightly extend along the x-axis by being "squeezed" by this positive radial force.

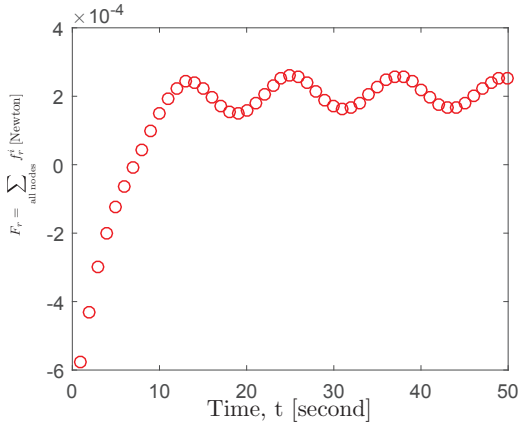

Figure S4: (a) Total radial force (summed over all the nodes), F_r, as a function of time, t.

S4 Measurement of buckling velocity in the simulations

A key component of the findings presented in the manuscript is the quantification of the critical angular velocity at which buckling occurs, ω_b. A simple way of measuring ω_b is to perform a parameter sweep along angular velocity, ω, where we increase ω at a *very slow rate* (e.g. 1 rpm per 1200 seconds for the representative case in the main manuscript) and record the suspended height, h. There is a sharp threshold on angular velocity at which the normalized suspended height, $\bar{h} = h/h_0$ (h_0 is the suspended height at $\omega = 0$), decreases from $\bar{h} \approx 1$ to $\bar{h} \approx 0.5$. This threshold value is taken to be the buckling velocity, ω_b.

However, the choice of this rate of increase of ω can affect the measurement of ω_b. This is especially true in Section V of the manuscript where our goal is to capture the rather small variation in buckling threshold as a function of the geometric parameters. Below, we introduce a rigorous method to measure ω_b based on the time required for a rod to buckle. The results presented in Section V were obtained using this protocol.

When an initially helical rod starts to rotate at an angular velocity, ω, that is greater than the buckling velocity, it will eventually buckle. We define the buckling time, τ, as the time taken for the normalized suspended height of the rod to fall below a critical value, which we set at $\bar{h} \leq 0.9$. In Fig. S5(a), we plot this buckling time, τ, as a function of ω for one of the rod configurations used in Fig. 8 of the manuscript (see caption for physical properties). We observe that the data is well described by

$$\tau = \frac{C_\tau}{\omega - \omega_b}, \tag{S6}$$

where ω_b is the buckling velocity and C_τ is a fitting parameter. Fitting the data in Fig. S5(a) to Eq. (S6) gives $\omega_b = 3.686 \pm 0.001$ rad/s and $C_\tau = 29.9 \pm 0.8$, where the uncertainties correspond to the 95% confidence interval of the fit. In Fig. S5(b), we present the same data to show τ versus $(\omega - \omega_b)$ with logarithmic axes, and find that all data points collapse on a straight line, which further supports the functional form in Eq. (S6).

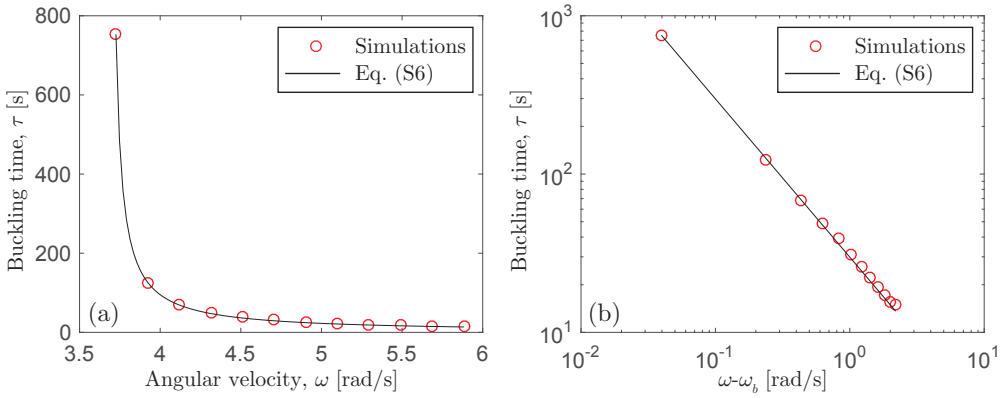

Figure S5: (a) Buckling time, τ, as a function of angular velocity, ω. Solid line corresponds to the fit to Eq. (S6). (b) Buckling time, τ, vs. $(\omega - \omega_b)$, with both axes in log scale. Material and fluid parameters are: pitch, $\lambda = 5.86$ cm, radius, $r_h = 0.794$ cm, axial length, $l = 14.64$cm, Young's modulus, $E = 1255$ kPa, cross-sectional radius, $r_0 = 1.577$ mm, viscosity, $\mu = 2.70$ Pa $\cdot$ s.